Self-consistent quasiparticle *GW* and hybrid functional calculations for Al/InAs/Al heterojunctions: Band offset and spin-orbit coupling effects

H. Ness,[1] F. Corsetti ,[2] D. Pashov,[1] B. Verstichel,[3] G. W. Winkler ,[4] M. van Schilfgaarde ,[1,5] and R. M. Lutchyn[4]

[1]*Department of Physics, Faculty of Natural and Mathematical Sciences, King's College London, Strand, London WC2R 2LS, England, United Kingdom*
[2]*Microsoft Azure Quantum, 2800 Lyngby, Denmark*
[3]*Synopsys Denmark, 2100 Copenhagen, Denmark*
[4]*Microsoft Azure Quantum, Goleta, California 93111, USA*
[5]*National Renewable Energy Laboratory, Golden, Colorado 80401, USA*

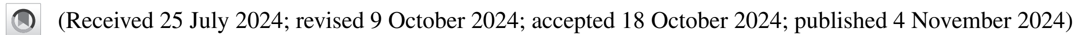
(Received 25 July 2024; revised 9 October 2024; accepted 18 October 2024; published 4 November 2024)

The electronic structure of surfaces and interfaces plays a key role in the properties of quantum devices. Here, we study the electronic structure of realistic Al/InAs/Al heterojunctions using a combination of density functional theory with hybrid functionals and state-of-the-art quasiparticle *GW* (QSGW) calculations. We find a good agreement between QSGW calculations and hybrid functional calculations, which themselves compare favorably well with angle-resolved photoemission spectroscopy experiments. Our paper confirms the need for well-controlled quality of the interfaces to obtain the needed properties of InAs/Al heterojunctions. A detailed analysis of the effects of spin-orbit coupling on the spin splitting of the electronic states shows a linear scaling in *k* space, related to the two-dimensional nature of some interface states. The good agreement by QSGW and hybrid functional calculations opens the door towards trustable use of an effective approximation to QSGW for studying very large heterojunctions.

DOI: 10.1103/PhysRevB.110.195301

I. INTRODUCTION

Because of their unique combination of material parameters (i.e., large spin-orbit coupling (SOC), small effective mass, large Landé *g* factor), narrow-gap III-V semiconductors (such as InAs or InSb) have generated considerable interest in many technological applications.

Recently, these materials have been central to the experimental realization of the so-called Majorana zero modes [1–10]. In these devices, the main goal is to develop topological *p*-wave superconductivity at the interface of a conventional semiconductor and an *s*-wave superconductor. An exceptionally good control of the interface properties is needed to realize topological superconducting phases and to manipulate Majorana zero modes, which are the key ingredient in topological quantum computation proposals [8,10–12]. The hybrid semiconductor-superconductor Majorana devices are required to have a large *g* factor, strong Rashba spin-orbit coupling, and significant proximity-induced superconducting gap. Recently, proximity-induced superconductivity has been studied in devices made of a semiconductor nanowire in contact with a superconductor, including Al/InAs [13–19], Al/InSb [20–23], Pb/InAs [24], and Sn/InSb [25]. High-quality superconductor/semiconductor interfaces (i.e., uniform and transparent) are required to optimize the topological gaps in these heterostructures.

The geometry of the interface may give rise to (desirable or undesirable) interface states, alter the band bending and band alignment, or affect the magnitude of the proximity-induced gap and of the spin-orbit coupling. Understanding the resulting surface/interface states and Fermi-level pinning is important for engineering appropriate interface Hamiltonians and realizing topological superconductivity hosting Majoranas.

Band bending and surface states have been observed by angle-resolved photoemission spectroscopy (ARPES) [26–28] and scanning tunneling microscopy and spectroscopy [29]. First principles simulations based on density functional theory (DFT) can help interpret experiments and resolve the effects of the interfaces. DFT studies of InAs and InSb surfaces and interfaces have been limited because local [local density approximation (LDA)] and semilocal exchange-correlation functionals severely underestimate the band gap to the limiting point where it reduces to zero [30]. More accurate methods involving quasiparticle self-consistent *GW* (QSGW) approaches or hybrid functionals provide results much closer to the experimental (bulk) gap (0.42 eV for bulk InAs).

In this paper, we present calculations of realistic Al(111)/InAs(001) heterojunctions using a QSGW method implemented in the QUESTAAL package. The QSGW results are also compared with hybrid functionals DFT calculations. We focus our attention on the effects of "disorder" (using numerical "experiments") on the electronic structure of

Published by the American Physical Society under the terms of the Creative Commons Attribution 4.0 International license. Further distribution of this work must maintain attribution to the author(s) and the published article's title, journal citation, and DOI.

realistic InAs/Al interfaces described at the atomic scale. The disorder we consider is coming from (i) atomic relaxations (i.e., the atoms at the InAs/Al interfaces do not rest at their corresponding bulk atomic positions), (ii) substitution disorder which mimics in a simple way potential atomic diffusion at the interface, and (iii) rescaling the spin-orbit coupling strength on some atoms which mimics the presence of some external electric fields at the interfaces.

The paper is organized as follows: In Sec. II, we present the InAs/Al system we considered and the two software packages used for the electronic structure calculations, namely the QUESTAAL and QUANTUMATK packages. The results of our calculations are shown and analyzed in Sec. III, where we extract the profiles of the valence band maxima (VBM) and conduction band minima (CBm) along the InAs/Al heterojunction and study in detail the effects of SOC on some specific bands. Conclusions are presented in Sec. IV. Additional information is provided in the Appendixes, about the implementation of the QUESTAAL code on GPUs in Appendix A, the hybrid functional in Appendix B, and local density of states and bulk versus heterojunction bands in Appendix C.

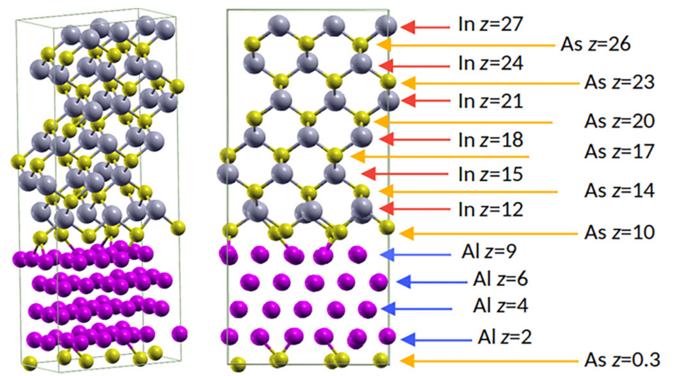

FIG. 1. Two sideviews, ball-and-stick representation, of the relaxed InAs(001)/Al(111) supercell. The In atoms are shown in gray, As atoms in yellow, and Al atoms in purple. The largest supercell contains 138 atoms with four, six, and seven atomic planes of Al, In, and As respectively. Each plane contains either six atoms of In (As) or 15 atoms of Al. The right panel shows the labeling, used in the main text, of the different atomic layers in the z direction.

II. CALCULATIONS

First principles electronic structure calculations have been performed using two different packages: the QUESTAAL package [31] and the pseudopotential QUANTUMATK package [32].

QUESTAAL is an all-electron method, with an augmented wave basis consisting of partial waves inside augmentation spheres based on the linear muffin-tin orbital technique [33]. It includes conventional DFT-based calculations, as well as many-body perturbation theory, especially with its implementation of a QSGW approach [34,35].

We have considered InAs/Al heterojunctions for which the interface between the two materials is built from the (001) surface for InAs and from the (111) surface for Al, with As-terminated InAs surfaces in direct contact with the Al surface (as suggested by the experiments in [27]). We took a low temperature lattice parameter of $a_0 = 6.06$ Å for InAl, and a (001) surface supercell based on the two following (001) surface vectors $u_1 = [2, 0]a_0$ and $u_2 = [-1, 3]a_0$. For this (001) supercell, there are six atoms in each In (As) atomic plane perpendicular to the z direction (see Fig. 1). For this supercell, one can match the Al(111) surface rather well, with a slight stretch (of 3%) in the u_2 direction, using a bulk lattice parameter of $a_{\rm Al} = 4.05$ Å. Then, each Al atomic plane parallel to the InAs/Al interface contains 15 atoms.

In order to minimize the computational cost, more specifically for the QSGW calculations, we have considered the minimal possible size for the junctions. We have found that to be able to keep the bulklike character for the electronic structure in the middle of the InAs slab, one needs to go beyond a few layers of InAl: typically for six (seven) atomic planes of In (As) (and beyond) we recover the bulklike density of states for the In (As) atoms in the center of the InAs slab. As Al is a metal with a shorter screening length, fewer atomic layers are needed [typically four atomic (111) planes are enough] to obtain a bulklike density of states in the central atomic layers (see Appendix C).

Relaxation of the atomic positions has been performed within DFT-LDA. We have allowed the atoms in the Al atomic layers next to the interfaces, and the atoms of As and In in the two outmost atomic layers close to the InAs/Al interfaces, to relax until the force components are below 10 mRy/bohr (257 meV/Å).

We did not impose any symmetry restrictions during the atomic relaxation. Therefore, since the two InAs/Al interfaces of the supercell are not symmetrically equivalent, the relaxation results in different local distortions at each interface. This allows us to minimize the possible existence of unwanted electronic states that may have arisen due to size and coupling effects between two identical interfaces. To some extent, this can be also seen as a simplified case of "geometric" disorder, for which the local environment of the relaxed atoms is different from the bulk. Hence, for such atoms, some form of spreading of the local density and potential will occur (in comparison to the bulk) as reflected in the extracted values of the local band edges shown below.

In DFT-LDA and even in GW calculations, band gaps are often underestimated (LDA) or overestimated (GW). Indeed they should be because the random phase approximation (RPA) screened Coulomb interaction W is not sufficiently screened. Improvement of W by the addition of ladder diagrams indeed does improve the gaps [36,37]. In most of the cases, the dielectric constant of semiconductors and insulators is about 80% of the experimental value. This is because the ladder diagrams are missing in the RPA. However, these higher order diagrams are computationally costly, and here we adopt a simpler approach. We have found that scaling the dielectric constant by 0.8, or alternatively using a hybrid of 80% QSGW and 20% LDA, we can mimic the effect of the ladders. This eliminates most of the errors. Hence, we use hybrid LDA and QSGW functionals, $\Sigma^{\rm scaled} = \Sigma_{\rm QSGW} \times 0.8 + V_{\rm xc}^{\rm LDA} \times 0.2$, in the calculations of our band structures.

The system we considered contains 138 atoms (4×15 atoms of Al, 6×6 of In, and 7×6 of As) [38]. In order to treat such a large system within QSGW calculations, the QUESTAAL package was redeveloped and optimized to take

advantage of GPU-based computing on a multipetaflop modular supercomputer (see Appendix A).

We are interested in determining the profile of the VBM and of the CBm along the InAs/Al heterojunction. There are different ways to find such a profile, for example by considering the electrostatic potential of the heterojunction, or by considering the change in energy position of deep electronic levels of the junction in comparison to their bulk equivalent. Obviously, the profile of the VBM or CBm obtained from such atomic scale systems (for example, the thickness of the InAs slab in the 138 atom supercell is ≈26.5 Å) will not reflect the band bending of Schottky barriers expected from a continuum model of the semiconductor/metal contact described on the micron scale. However our atomic scale calculations incorporate the more local effects of the InAs/Al interfaces against the bulk property of the materials.

To evaluate the profile of the valence (conduction) band maxima (minima), we extract the energy position of the deep electronic levels on each In atom (deep d orbital) and each As atom (deep s orbital). Assuming a rigid energy shift of these deep electronic levels relative to the Fermi level E_F in both the bulk and the heterojunction systems, we can determine the profile (averaged over the number of atoms in each atomic layer) of the VBM (along the main direction of the junction) relative to the exact QSGW Fermi level of the junction. The profile of the CBm is obtained from a rigid shift of the VBM by the bulk QSGW band gap (0.47 eV in the present case).

It is important to note that all the QSGW calculations were performed in the presence of SOC. Orbitals with s-like character are not affected by the presence of SOC. However the d orbitals are split by the SOC. For a bulklike environment, the d orbitals are split into two subsets according to the crystal symmetry. For In atoms close the Al/InAs interfaces the symmetry is reduced (further reduced by the atomic relaxations), and different energy shifts occur for the different d orbitals on these atoms. There is more "fluctuation" of the energy shift for these atoms in comparison to bulklike In atoms in the center of the InAs slab.

As a final comparison, we also perform calculations on the same system using a different methodology for correcting the band gap problem: hybrid functionals. Traditional hybrid functionals which use a fixed global mixing fraction α of Fock exchange can show limitations in the case of inhomogeneous interface systems, specifically if the different materials require different values of α to recover the correct bulk electronic structure and band gap. The situation is even more severe for the present case of semiconductor/metal interfaces.

To overcome this problem, we build on a recently developed scheme for a local (i.e., spatially varying) mixing fraction, based on an estimator of the local dielectric constant defined as a functional of the electronic density [39,40]. In order to deal with the metallic region in our system, a second, metallic, estimator is introduced, which determines locally if the material is a metal and, if so, sets α to zero. A more detailed explanation of the method can be found in Appendix B. We apply this scheme to the HSE06 functional [30]. We shall refer to these calculations as HSE06+DDH (dielectric-dependent hybrid).

The HSE06+DDH calculations are performed using the QUANTUMATK package [32] (version T-2022.03) within a pseudopotential and linear combination of atomic orbitals (LCAO) formalism. The calculations are carried out with a spin-polarized noncollinear Hamiltonian. We use norm-conserving pseudopotentials from the PSEUDODOJO [41] fully relativistic set and the medium basis set (LCAO-M [32]) from QUANTUMATK. The auxiliary density matrix method [42] is used to speed up the calculation of the exchange matrix. A k-point grid of $(4 \times 4 \times 2)$ for the interface system is used to match the QSGW calculations.

The determination of the VBM/CBm is performed in the same way as for the QSGW calculations, i.e., by extracting the energy position of the core levels relative to E_F. However, due to the configuration of the pseudopotentials, we use the semicore d orbitals for both In and As. The bulk InAs band gap obtained with HSE06+DDH is 0.47 eV, in agreement with QSGW.

III. RESULTS

A. Band alignment

Figure 2 shows the profile of the VBM in the InAl/Al heterojunctions (black dashed line for the QSGW calculations, and black dashed-dotted line for the LDA calculations). It corresponds to a shallow paraboliclike curve where the VBM is higher close to the InAs/Al interfaces than in the bulklike part of InAs. Such a profile does not directly compare with conventional band bending in Schottky barriers; the latter occurs on much larger length scales ($\approx \mu$m) than the scale corresponding to our atomic-scale calculations. However, the inflection of the VBM reflects the effect of the interfaces against the bulk, most certainly due to the presence of interface electric dipoles.

The dispersion in the energy shifts displayed by the symbols (red circles for the In deep d orbital, green up triangles for the As deep s orbital obtained from the QSGW calculations) reflects that each atom in a given atomic layer is different. This is mostly true for the atoms near the InAs/Al interfaces which have been allowed to relax. Such a dispersion is minimal for the atoms in the center of the InAs slab where their positions correspond to bulk unrelaxed atomic positions.

The QSGW calculation for bulk InAs provides a band gap 0.47 eV, close to the experimental band gap of 0.42 eV at low temperature. From that value, we can see that the CBm (obtained from rigid shift of the VBM) crosses the Fermi level of the junction. The CBm lies below E_F, by an amount of ≈ 80 meV, in the "bulk" part of the InAs slab. This prediction of an accumulation layer in InAs is in agreement with ARPES measurements [27], although the band offset extracted from experiment is somewhat larger than what is seen in the present cell simulation. This may be related to finite size effects or the other InAs/Al interface effects. We explore one possibility in the following.

But for now, we turn to our hybrid functional calculations using the HSE06+DDH method. This method represents a more empirical and less accurate approach than QSGW, but also significantly less demanding of computational resources, and therefore potentially able to scale to larger systems. Figure 3 shows the comparison of the local band edges calculated with QSGW (solid lines) and HSE06+DDH (filled

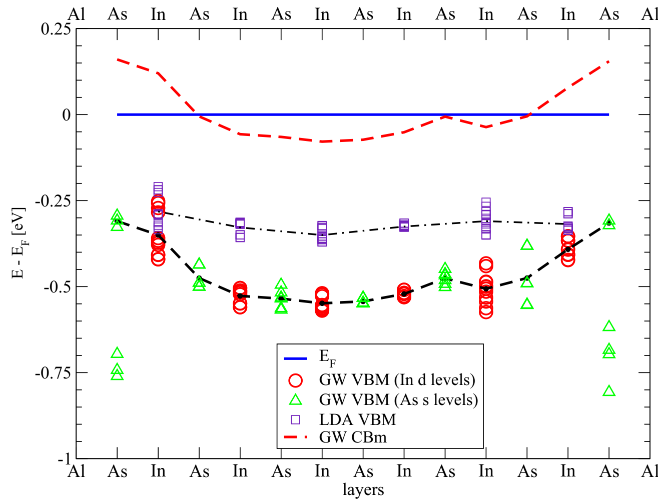

FIG. 2. Profile of the local valence band maximum (VBM) for the InAs/Al junction made of 138 atoms. Symbols represent the different shifted energy levels (deep In-*d* and As-*s* orbitals) of the In and As atoms located in each atomic plane along the main axis of the junction. Lines correspond to the averaged value of the energy shift in each atomic plane. The black dashed and dashed-dotted lines correspond to the QSGW and LDA VBM respectively. The red dashed line is the QSGW conduction band minima (CBm), i.e., the VBM shifted by the QSGW bulk band gap. The blue line presents the Fermi level E_F position. Both QSGW and LDA have been shifted to correspond to this energy reference $E_F = 0$. The QSGW CBm lies ≈ 80 meV below E_F in the center of the InAs slab. Note that the band profile is not symmetric with respect to the central As layer because the left and right InAs/Al interfaces are not symmetrically equivalent, and the atomic relaxation increases the asymmetry.

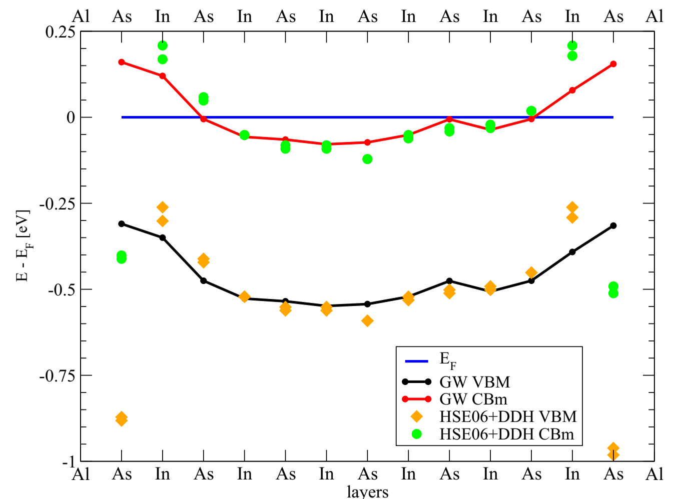

FIG. 3. Profile of the local VBM and CBm for the InAs/Al junction obtained from QSGW (same averaged values as in Fig. 2) and HSE06+DDH.

circles). The overall shape of the band edges is well reproduced by HSE06+DDH, and there is an excellent quantitative agreement in the bulk of the semiconductor (within two layers of the interface). The last layer of As atoms at the interface with Al deviates both from the smooth profile and from the QSGW result (however, it should be noted that the complete QSGW data set in Fig. 2 shows a qualitatively similar discontinuity for the majority of As atoms at the interface). These uncertainties are not surprising, as the use of core levels to extract the band edges depends on a sufficiently bulklike local environment, while the last layer is expected to deviate significantly due to the different bonding.

As an additional check, we have also compared the LDA band edges calculated with the package QUESTAAL (shown in Fig. 2) with QUANTUMATK (not shown) and recovered a similar good agreement. Therefore, the HSE06+DDH method provides an effective approximation to the full QSGW for this system, and might be used to explore much larger interface cells or multiple different interface configurations at a lower computational cost.

In order to get a better understanding of the effects of disorder at the InAs/Al interfaces on the energy level alignment, we have considered the following numerical experiment.

We simulate the possible atomic diffusion at the interfaces by substituting some atoms by others. From the valence properties of In, As, and Al, it appears reasonable to envisage substitutional disorder between In and Al atoms. Furthermore, previous molecular beam epitaxy experiments have shown that AlAs can be readily grown as a thin interlayer at the InAs/Al interface [13]. We have therefore considered interfaces for which some In atoms (in the atomic layers closest to the interfaces) are replaced by Al atoms.

There are many possible combinations to realize such substitutions, and we have considered only a few of them. We started by replacing only one In atom by one Al atom in the In atomic layer located the closest to the right InAs/Al interface (see labels for the atomic planes in Fig. 4). We have performed calculations for only two cases over the six possible cases of one atom substitution. The results for the VBM profile for one of these cases is shown in Fig. 4 by the black dashed line. We have also considered one case in which two In atoms are swapped by two Al atoms and we have found similar trends for the profile of the VBM (results not shown here). Our calculations indicate that the VBM is pushed down, by a further ≈ 100 meV, to lower energy in the case of the "dirty" interfaces compared to the case of "perfect" interfaces.

B. Spin-orbit coupling effects

The presence of Rashba-like SOC in narrow-gap InAs semiconductors is one of the central ingredients for inducing a superconducting property by proximity of an *s*-wave superconductor like Al. Once superconducting, a InAs nanowire can eventually host a pair of Majorana states at each of its ends where the superconducting order parameter vanishes.

In the previous section, we have studied how band alignment in InAs deviates from pure bulk to InAs/Al interfaces, including some form of disorder of the interfaces. We now consider the possibility of another type of disorder and its effects on the band structure of the InAs/Al junction.

For that we now consider the following numerical experiment: the strength of the SOC, on some atoms in the system, is rescaled to larger values. The SOC rescaling is applied on either all the In and As atoms or only the In and As

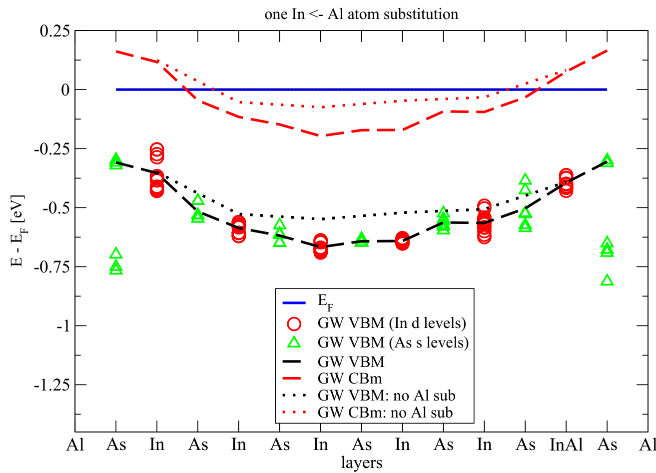

FIG. 4. Profile of the local valence band maximum (VBM) for the InAs/Al junction with similar notations as in Fig. 2. Comparison between perfect and disordered interfaces nis shown. One atom of In is replaced by one Al atom in the In atomic plane closest to the right InAs/Al interface (see label InAl on the horizontal axis). All calculations are performed with QSGW. The VBM/CBm are pushed down to lower energy in the case of the dirty interface, i.e., compare dashed lines with dotted lines (black for VBM, red for CBm). Interface disorder seems to push the CBm down by a further ≈100 meV. A similar behavior has also been obtained in two different cases of one In ← Al atom substitution (the Al atom is located at a different site in the corresponding In atomic plane), as well as for a case of two In ← Al atoms substitution in the corresponding In atomic plane (results not shown here).

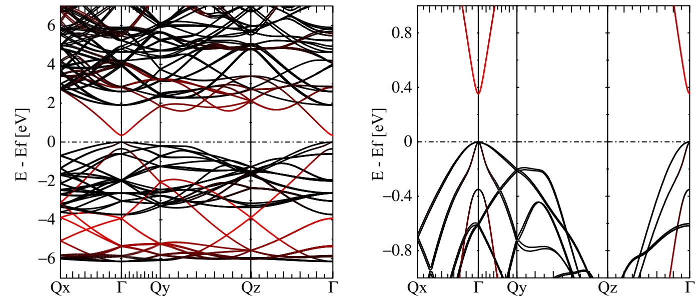

FIG. 5. QSGW bulk band structure of InAs (including SOC). Left panel: Wide energy range. Right panel: Energy range closer to the Fermi level E_F. For allowing direct comparisons between bulk and heterojunctions, the bulk bands have been calculated with a cell having the same lattice vectors $u_{1,2}$ in the (001) plane as the cell for the InAs/Al junction. Qx, y, z represents the (x, y, z) direction in the reciprocal space. The color scheme corresponds to the weight of the As s orbital in the bands, i.e., bright red indicates large weight of the As s orbital, where less bright red means less weight, down to black, which means no As s-orbital weight. One can see that the bottom of the conduction band is mostly consisting of As s states.

atoms close to the InAs/Al interfaces, i.e., In atoms labeled $z = 12$ and 27 and As atoms labeled $z = 0.3$ and 10 (see right panel in Fig. 1). Note that a light element like Al does not have strong SOC and rescaling the SOC on Al is not relevant. The increase of the SOC can be seen as an indirect effect of the presence of an extra external electric field (perpendicular to the InAs/Al interface in the case of Rashba-like SOC) due to gating or other effects not taken into account in our model of heterojunctions. We analyze the effects of rescaling the SOC on a specific set of bands which we identify to be the counterpart of the bottom of the bulk InAs conduction band, as we explain below.

But first, we show how the band structure of the InAs/Al junction differs strongly from the bulk InAs bands due to the coupling to the metallic As states. Figure 5 shows the bulk band structure of InAs. To be able to compare directly bulk and junction band structures, we have calculated the bulk bands with a cell having the same lattice vectors $u_{1,2}$ in the (001) plane as the cell for the InAs/Al junction. The bottom of the conduction band around the Γ is mostly consisting of As s states as expected. The color scheme in Fig. 5 will allow us to identify the corresponding bulklike InAs conduction band in the band structure of the heterojunction.

For the InAs/Al junction, most of the bands in the junction come from a mixture of all In, As, and Al orbitals as can be seen in Fig. 6. This can be expected from the strong bonding between the InAs semiconductor and the Al metal parts in our model of heterojunction. The band structure looks much more complex than for bulk InAs due to the large size of the system, the presence of the Al metallic states, and the relaxation of the InAs/Al interfaces. There is clearly no band gap anymore in the heterojunction.

Figure 7 shows the zoomed-in energy of the bands shown in Fig. 6. The bands are colored in red according to the projection weight of the states onto the s orbitals of the bulklike atomic layers of As $z = 20$. In Fig. 5, it was shown that the bottom of the bulk InAs conduction band, around the Γ point, is mostly of As s character. For the InAs/Al heterojunction, we can infer that some bands around the Γ point still keep a non-negligible weight of the bulklike As s orbitals, more specifically the bands ≈50 meV below E_F. This energy position below E_F corresponds well with our estimate of the energy shift of the bulklike conduction band minimum shown in Fig. 2. We therefore consider that these bands are the equivalent of the bottom of the bulklike conduction band of InAs which strongly couples to the Al states in the InAs/Al heterojunction. We now study how these bands are modified by the rescaling of the strength of the SOC. For that, we calculate the energy difference $\Delta E(k)$ between these SOC spin-split bands for different SOC rescalings.

Figure 8 shows the energy difference $\Delta E(k)$ of the spin-split bands around the Γ point versus the k vector along the Γ-Qy direction. The spin splitting is more important (for small k values away from Γ) when the SOC rescaling is applied to all In and As atoms, instead of only on the interface In and As atoms. However, it is clear that, in both cases, the spin splitting $\Delta E(k)$ is linear in k (for $k/Qy < 0.1$), which is most probably the signature of the two-dimensional-like character of the corresponding states parallel to the InAs/Al interface [43,44]. The main point is that the interface gives rise to large electric fields, which can yield Rashba-like terms within a few atomic planes of the interface; these Rashba-like terms then cause the linear in k splitting of states there.

It is also interesting to check how the linear dependence of the spin splitting varies with the rescaling of the SOC.

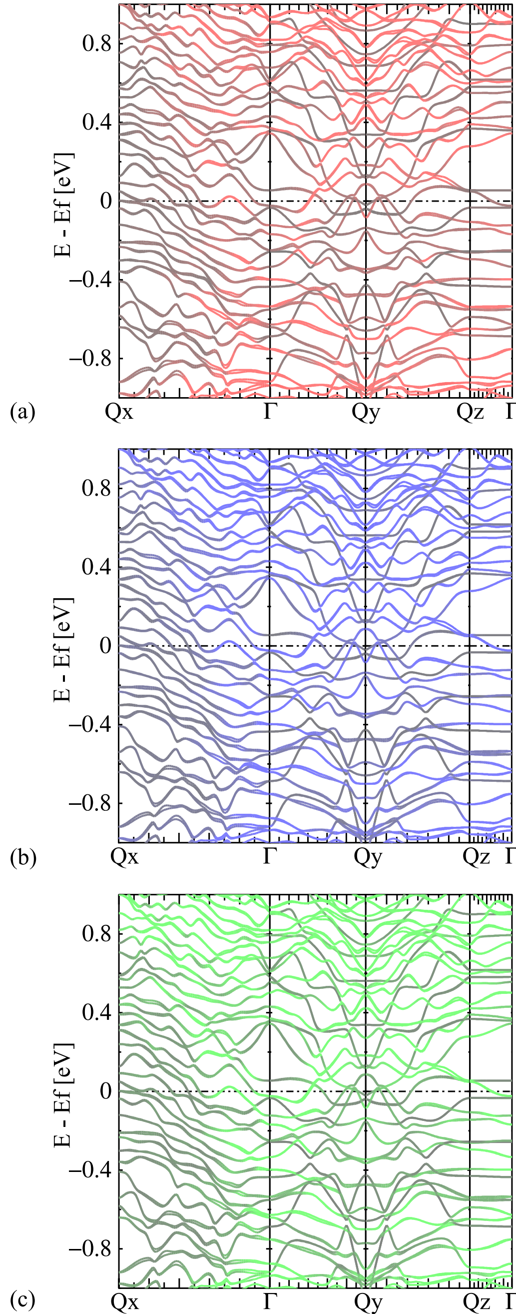

FIG. 6. QSGW band structure of the InAs/Al heterojunction made of 138 atoms. In comparison to the bulk InAs case, the band structure is more complicated due to the presence of the Al metallic states, the relaxation of the InAs/Al interfaces, and the large number of atoms in the supercell. There is no more band gap in the heterojunction. The bands in panels (a), (b), and (c) are colored in red, blue, and green respectively according to the projection weight of the states onto the bulklike atomic layers of As $z = 20$, In $z = 18$, and In $z = 21$. There is a strong mixing of all As and In orbitals in the bands, as well as mixing with Al orbitals. Note the two flat bands around $E_F = 0$ along the Γ-Qz direction implying the existence of localized “interface” states. These states are however delocalized in the (xy) planes of the InAs/Al interfaces. A careful analysis of the composition of these states (not shown here) reveals that they consist mostly of orbitals of the As $z = 10$ and Al $z = 9$ (and of the As $z = 0.3$ and Al $z = 2$) atomic layers.

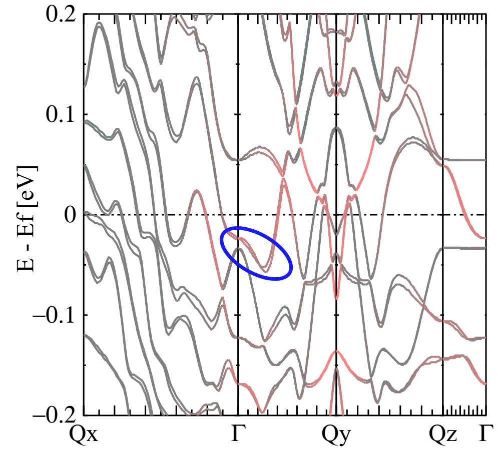

FIG. 7. QSGW band structure of the InAs/Al heterojunction: zoomed-in energy of the bands shown in Fig. 6. Here the red coloring scheme follows the weight of the projection onto the s orbitals of the bulklike central atomic layer of As $z = 20$. Some bands around Γ, in the heterojunction, keep a non-negligible weight of the bulklike As s orbitals, more specifically the bands $\approx$50 meV below E_F. Knowing that the bottom of the bulk InAs conduction band, around the Γ point, is mostly made of As s character, we consider that these bands (encircled in blue) correspond to the bottom of the bulk InAs conduction band in the case of the junction.

We determine the slope of the linear relation $\Delta E(k) \equiv \alpha k$ for small k values (for $k/Qy < 0.05$). The dependence of α(socscl) on the SOC rescaling is shown in Fig. 9. We obtain a linear dependence on SOC rescaling when the rescaling is applied to all In and As atoms, and a sublinear dependence when the rescaling is only applied to the interface In and As atoms, indicating different screening effects on the local SOC rescaling.

IV. CONCLUSION

We have studied the electronic structure of realistic Al/InAs/Al heterojunctions using a combination DFT with hybrid functionals and state-of-the-art QSGW calculations. The InAs/Al heterojunctions we considered are central to superconducting induced properties in InAs and to the design of topological quantum computation platforms. The InAs/Al heterojunctions are described at the atomic level and include atomic relaxations at the InAs/Al interfaces. Our paper confirms the need for well-controlled quality of the interfaces to obtain the needed properties of InAs/Al heterojunctions. The local band alignment (i.e., top of VB, bottom of CB) obtained from QSGW for semiconductor/metal interfaces can be well reproduced using dielectric-dependent hybrid functional DFT with the metallic estimator which automatically switches off the Fock exchange within the bulk of the metal. The prediction of an accumulation layer for InAs/Al is in agreement with experimental evidence. The HSE06+DDH method appears to provide an effective approximation to the full QSGW for this system, and opens paths for exploring larger interface cells or multiple different interface configurations in relation with experimental devices. Furthermore, a detailed analysis of the effects of spin-orbit coupling on the spin splitting of some electronic states shows a linear scaling in k space, a

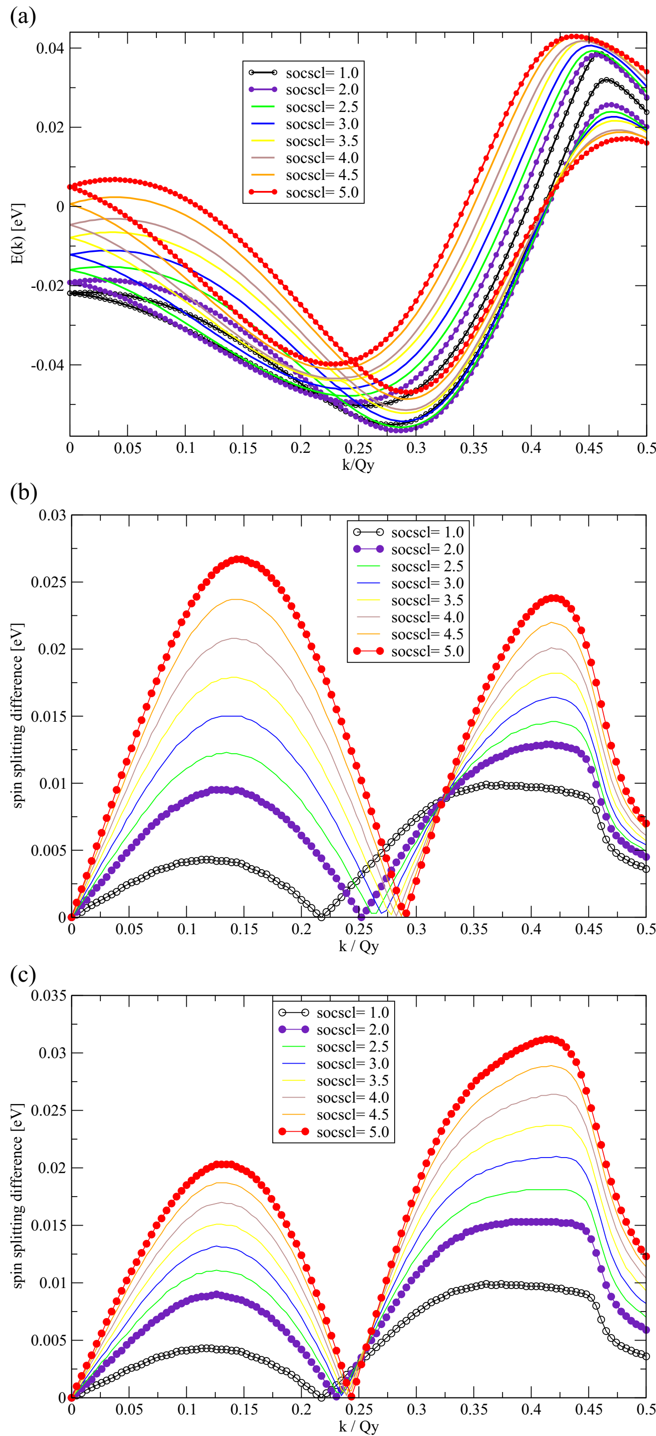

FIG. 8. (a) Bands around the Γ point, in the Γ-Qy direction, corresponding to the bands encircled in blue in Fig. 7 calculated for different rescaling (socscl) of the SOC. The rescaling is applied to all In and As atoms. (b) Energy difference $\Delta E(k)$ of the spin-split bands shown in panel (a). (c) Energy difference $\Delta E(k)$ of the spin-split bands when the rescaling socscl is applied only to the In and As interface atoms. In both cases, the spin splitting is linear in k for $k/Qy < 0.1$ around each band crossing, i.e., $\Delta E(k) \equiv \alpha k$.

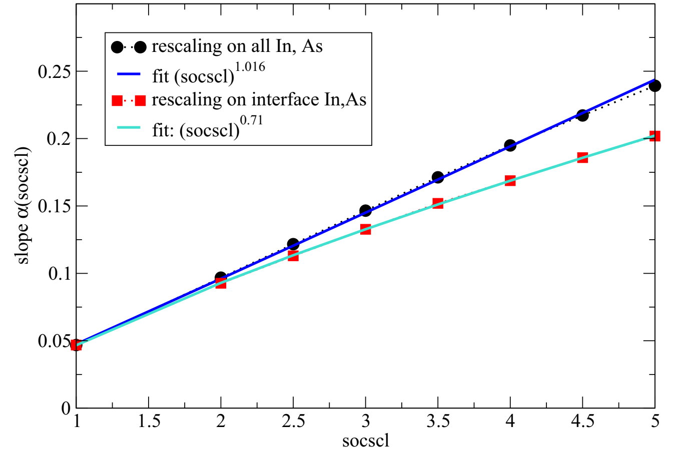

FIG. 9. Dependence of the slope α of $\Delta E(k) \equiv \alpha k$ upon the rescaling socscl of the SOC. A linear dependence on the rescaling is obtained when it is applied to all In and As atoms, while a sublinear dependence is obtained when the rescaling is applied only to the interface In and As atoms.

behavior most probably related to the two-dimensional nature of the interface states. Our paper indicates the possibility of tailoring the properties of the electronic states central to the realization of topological computers from the quality of the semiconductor/metal interface.

ACKNOWLEDGMENTS

This work was authored by the National Renewable Energy Laboratory, operated by Alliance for Sustainable Energy, LLC, for the U.S. Department of Energy under Contract No. DE-AC36-08GO28308, funded by Office of Science, Basic Energy Sciences, Division of Materials. We acknowledge the use of the National Energy Research Scientific Computing Center (NERSC), under Contract No. DE-AC02-05CH11231 using NERSC Grant No. BES-ERCAP0021783, and we also acknowledge that a portion of the research was performed using computational resources sponsored by the Department of Energy's Office of Energy Efficiency and Renewable Energy and located at the National Renewable Energy Laboratory. For early stages of this work, H.N. and M.v.S. acknowledge financial support from Microsoft Station Q via a sponsor agreement between KCL and Microsoft Research. H.N., D.P., and M.v.S. acknowledge the Partnership for Advanced Computing in Europe for awarding us access to Juwels Booster and Cluster (Jülich, Germany).

APPENDIX A: QUESTAAL ON GPU

Due to the relatively large simulation cell for QSGW standards, together with (i) relatively dense Brillouin zone sampling and (ii) high angular momentum cutoffs required, the all-electron full frequency QSGW calculations are rather difficult to achieve. They were only made practical with the efficient use of new clusters with high-density, high-memory GPU nodes and good interconnect.

Algorithmic improvements avoided most of the filesystem IO. Together with a more flexible memory management, they allowed efficient parallelization across multiple levels of processes and threads enabling various launch configurations. Nearly all of the remaining IO was moved to parallel

HDF5 maintaining the same file layout independent of the parallelism.

The screened Coulomb potential and the mixed product basis projectors occupy the bulk of the memory available and in the present case could not fit together entirely; fortunately the projectors can be generated and used in piecewise fashion with little overhead.

In the GPU context, each device is handled by a thread allowing simple use of multiple devices per process. The threads distribute batches of matrix operations across dynamically estimated number of streams depending on dimensions and the available memory. In this way host-device transfers and kernel launches are overlapped through asynchronous executions, hiding latency and maximizing occupancy and efficiency.

Most of the computing routines make heavy use of the performance libraries CUBLAS, CUSOLVER, CUFFT, and CUSPARSE in this mode. Certain larger matrix operations were done collectively with CUSOLVERMG (CU*MP was not available at the time).

The heaviest step in the computations is the calculation of the full off-diagonal self-energy, which sustained close to 20 petaflops on the Juwels-Booster cluster using 288 nodes.

APPENDIX B: LOCAL DDH FUNCTIONAL WITH METALLIC CORRECTION USING LOCALIZED ORBITALS

1. DDH overview

The exchange-correlation energy in HSE is constructed by splitting up the Coulomb interaction in a long and short range part using the error functions

$$\frac{1}{r} = \frac{\mathrm{erf}(\omega r)}{r} + \frac{\mathrm{erfc}(\omega r)}{r},$$

in which ω is a range separation parameter that determines what is defined as long and short range. The exchange correlation energy is then split up as

$$E_{xc}^{\mathrm{HSE}} = \alpha E_x^{\mathrm{HF,SR}} + (1-\alpha)E_x^{\mathrm{PBE,SR}}(\omega) + E_x^{\mathrm{PBE,LR}}(\omega) + E_c^{\mathrm{PBE}}.$$

The amount of *exact* exchange included is determined by α, the exchange fraction. In HSE it is taken to be a constant of 0.25, which is reasonably accurate for medium gap semiconductors but produces some errors for large and small gaps. This is because one can derive that the value of α should be related to the dielectric constant of the material, which is in turn related to the screening. The DDH approach is to create a hybrid functional for which the exchange fraction is determined self-consistently based on the dielectric constant. This is too computationally expensive to calculate, and so an estimator for the dielectric function is used instead (as presented in [39,40]):

$$\bar{g} = \frac{1}{V}\int d\mathbf{r}\sqrt{\frac{\nabla\rho(\mathbf{r})}{\rho(\mathbf{r})}}.$$

The exchange fraction is then related to this estimator by a quartic function:

$$\alpha_{\mathrm{DDH}} = a_0 + a_4\bar{g}^4,$$

which we have fitted to the correct experimental band gap for a large set of semiconductors and insulators.

2. Local DDH using localized orbitals

To study interfaces, it might be that different values of the exchange fraction are needed in different parts of the system. This is why a local estimator is introduced:

$$\bar{g}(\mathbf{r},\sigma) = \frac{1}{(2\pi\sigma)^{\frac{3}{2}}}\int d\mathbf{r}'\sqrt{\frac{\nabla\rho(\mathbf{r}')}{\rho(\mathbf{r}')}}\exp\left(-\frac{|\mathbf{r}-\mathbf{r}'|^2}{2\sigma}\right),$$

from which we can calculate an exchange fraction field

$$a(\mathbf{r},\sigma) = a_0 + a_4\bar{g}(\mathbf{r},\sigma)^4.$$

In [40] this is used in the calculation of the integrals, so that the exchange matrix becomes

$$X_{ij} = \sum_{kl} V_{ik;jl}D_{kl},$$

in which D_{kl} is the single-particle density matrix. The coulomb integrals are defined as

$$V_{ik;jl} = \int d\mathbf{r}d\mathbf{r}'\phi_i(\mathbf{r})\phi_k(\mathbf{r})\alpha(\mathbf{r},\mathbf{r}';\sigma)K(|\mathbf{r}-\mathbf{r}'|)\phi_j(\mathbf{r}')\phi_l(\mathbf{r}'),$$

in which ϕ_i are the LCAO basis orbitals, with

$$\alpha(\mathbf{r},\mathbf{r}';\sigma) = \sqrt{a(\mathbf{r},\sigma)a(\mathbf{r}',\sigma)}$$

and K the short range Coulomb kernel.

Instead of recalculating the integrals we use the fact that in QUANTUMATK a resolution of identity [45] approach is used to calculate the Coulomb integrals:

$$V_{ik;jl} \approx C_{ik}^{\mu}V_{\mu\nu}C_{jl}^{\nu},$$

with the introduction of an auxiliary basis $P_\mu(\mathbf{r})$ such that

$$\phi_i(\mathbf{r})\phi_j(\mathbf{r}) = \sum_{\mu} C_{ij}^{\mu}P_\mu(\mathbf{r}).$$

We assume that the auxiliary basis coefficients C_{ij}^{μ} are unaffected, and only the integrals between the auxiliary basis functions change,

$$\begin{aligned} V_{\mu\nu} &= \int d\mathbf{r}d\mathbf{r}'P_\mu(\mathbf{r})\alpha(\mathbf{r},\mathbf{r}';\sigma)K(|\mathbf{r}-\mathbf{r}'|)P_\nu(\mathbf{r}') \\ &\approx \sqrt{\bar{a}_\mu\bar{a}_\nu}\int d\mathbf{r}d\mathbf{r}'P_\mu(\mathbf{r})K(|\mathbf{r}-\mathbf{r}'|)P_\nu(\mathbf{r}'), \end{aligned}$$

in which we have taken a Gaussian average of the a coefficients around the center they are located on:

$$\bar{a}_\mu(\sigma,\tau) = \int d\mathbf{r}a(\mathbf{r},\sigma)\exp\left(-\frac{|\mathbf{r}-\mathbf{r}_\mu|^2}{2\tau}\right). \tag{B1}$$

The approximation being made here is that the local estimator is approximately constant or at least slowly varying over the region where a single auxiliary basis function has support, which is on a center.

3. Metallic correction to local DDH

For metals there is perfect screening, and we would expect the exchange fraction to go down to zero. Unfortunately the DDH method does not reproduce this behavior. This is why we introduce a second *metallic* estimator. At every step of

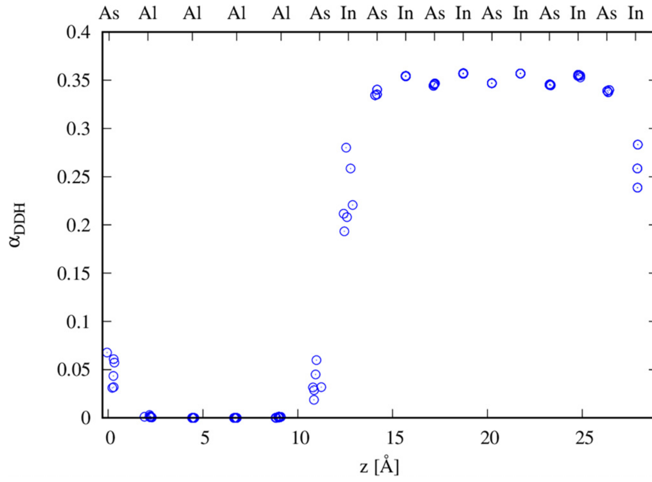

FIG. 10. The local exact exchange fraction on each atomic center obtained with the HSE06+DDH method for the InAs/Al heterojunction.

the self-consistent loop we calculate the Fermi level density matrix

$$\mathcal{F}_{ij} = \sum_{\mathbf{k}} \sum_{n} \exp\left[-\frac{(\epsilon_F - \epsilon_{\mathbf{k},n})^2}{2\sigma_F}\right] \langle \phi_i | \psi_{\mathbf{k}n} \rangle \langle \psi_{\mathbf{k}n} | \phi_j \rangle,$$

where $\psi_{\mathbf{k}n}$ are the Kohn-Sham eigenstates at the current step in the self-consistent field (SCF) loop and σ_F is the Fermi level broadening, chosen to be 0.001 eV. The Fermi level density matrix is used to calculate the Fermi level density:

$$f(\mathbf{r}) = \sum_{ij} \mathcal{F}_{ij} \phi_i(\mathbf{r}) \phi_j(\mathbf{r}).$$

We then define the following metallic estimator function:

$$M(\mathbf{r}) = 1 \quad \text{if} \quad f(\mathbf{r}) < c_\mu,$$
$$M(\mathbf{r}) = 0 \quad \text{if} \quad f(\mathbf{r}) \geqslant c_\mu,$$

where c_μ is a cutoff parameter we have chosen to be 0.0003. This parameter in combination with σ_F determines what parts of the material will be identified as metallic. They have been chosen empirically after extensive testing on a wide variety of materials.

This function is convoluted with a Gaussian to get a smooth metallic estimator function:

$$m(\mathbf{r}) = \int d\mathbf{r}' M(\mathbf{r}') \exp\left(-\frac{|\mathbf{r} - \mathbf{r}'|^2}{2\sigma_\mu}\right),$$

where the width of the Gaussian is chosen to be 1 Å by default, which we have found to give stable and smooth convergence of the SCF loop; the final simulations in this paper were checked with respect to this parameter, showing a weak dependence on the smoothing length. We then multiply the metallic estimator with the function $a(\mathbf{r}, \sigma)$:

$$a_m(\mathbf{r}, \sigma) = m(\mathbf{r}) a(\mathbf{r}, \sigma),$$

before the averaging around a center is performed in Eq. (B1).

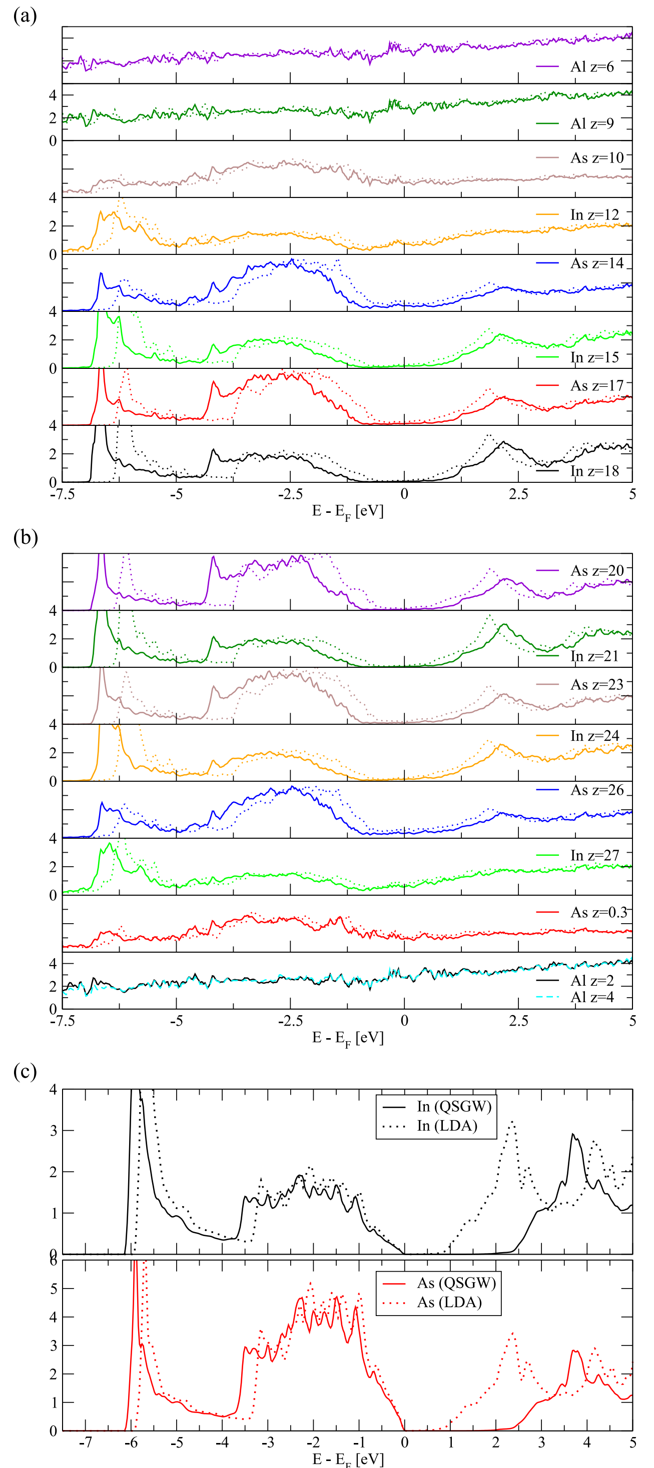

FIG. 11. (a), (b) Local density of states (LDOS) per atomic layer in the InAs/Al heterojunction, obtained from QSGW (solid lines) and LDA (dotted lines) calculations. (c) Corresponding bulk LDOS for In and As atoms respectively. In panels (a) and (b), the LDOS of the central In and As atomic layers, labeled $z = 18, 20, 21$, are similar to the bulk LDOS. The LDOS of the In and As atomic layers acquires a stronger admixture with the Al states, the closer the layers are to the InAs/Al interfaces. Note that in the bulk LDOS, the Fermi energy E_F is located at the top of the valence band as a convention for any semiconductors at zero temperature. For the heterojunction, the position of E_F is governed by the metallic states of the Al slab.

4. Application to the InAs/Al heterojunction

Figure 10 shows how the local DDH scheme with the addition of the metallic estimator described here results in a smoothly varying α for the semiconductor/metal interface system of interest. The mixing fraction is close to zero in the metallic Al layers, and then transitions to a finite value for InAs over two layers of the semiconductor. It can be seen that the DDH scheme results in a value of α for InAs that is significantly increased by 41% with respect to the default value of 0.25, resulting in a more accurate band gap. Furthermore, even within the bulk of the semiconductor the DDH gives a locally varying α, with a difference of $\approx$0.01 between the In and As layers.

APPENDIX C: LOCAL DENSITY OF STATES

In Fig. 11, we show the LDOS per atomic layer in the InAs/Al heterojunction, with the labeling of the different atomic planes defined in Fig. 1. One can see that the LDOS of the central In and As atomic layers, labeled $z = 18, 20, 21$, is very similar to the bulk LDOS.

[1] J. D. Sau, R. M. Lutchyn, S. Tewari, and S. Das Sarma, Generic new platform for topological quantum computation using semiconductor heterostructures, Phys. Rev. Lett. **104**, 040502 (2010).

[2] J. Alicea, Majorana fermions in a tunable semiconductor device, Phys. Rev. B **81**, 125318 (2010).

[3] R. M. Lutchyn, J. D. Sau, and S. Das Sarma, Majorana fermions and a topological phase transition in semiconductor-superconductor heterostructures, Phys. Rev. Lett. **105**, 077001 (2010).

[4] Y. Oreg, G. Refael, and F. von Oppen, Helical liquids and Majorana bound states in quantum wires, Phys. Rev. Lett. **105**, 177002 (2010).

[5] J. Alicea, New directions in the pursuit of Majorana fermions in solid state systems, Rep. Prog. Phys. **75**, 076501 (2012).

[6] M. Leijnse and K. Flensberg, Introduction to topological superconductivity and Majorana fermions, Semicond. Sci. Technol. **27**, 124003 (2012).

[7] C. Beenakker, Search for Majorana fermions in superconductors, Annu. Rev. Condens. Matter Phys. **4**, 113 (2013).

[8] S. Das Sarma and M. Freedman, Majorana zero modes and topological quantum computation, npj Quantum Inf. **1**, 15001 (2015).

[9] R. Aguado, Majorana quasiparticles in condensed matter, Riv. Nuovo Cimento **40**, 523 (2017).

[10] R. M. Lutchyn, E. P. A. M. Bakkers, L. P. Kouwenhoven, P. Krogstrup, C. M. Marcus, and Y. Oreg, Majorana zero modes in superconductor-semiconductor heterostructures, Nat. Rev. Mater. **3**, 52 (2018).

[11] C. Nayak, S. H. Simon, A. Stern, M. Freedman, and S. Das Sarma, Non-Abelian anyons and topological quantum computation, Rev. Mod. Phys. **80**, 1083 (2008).

[12] M. Aghaee, A. A. Ramirez, Z. Alam, R. Ali, M. Andrzejczuk, A. Antipov, M. Astafev, A. Barzegar, B. Bauer, J. Becker, U. K. Bhaskar, A. Bocharov, S. Boddapati, D. Bohn, J. Bommer, L. Bourdet, A. Bousquet, S. Boutin, L. Casparis, B. J. Chapman, S. Chatoor, A. W. Christensen *et al.*, Interferometric single-shot parity measurement in an InAs-Al hybrid device, arXiv:2401.09549.

[13] P. Krogstrup *et al.*, Epitaxy of semiconductor-superconductor nanowires, Nat. Mater. **14**, 400 (2015).

[14] H. J. Suominen, M. Kjaergaard, A. R. Hamilton, J. Shabani, C. J. Palmstrøm, C. M. Marcus, and F. Nichele, Zero-energy modes from coalescing Andreev states in a two-dimensional semiconductor-superconductor hybrid platform, Phys. Rev. Lett. **119**, 176805 (2017).

[15] F. Nichele, A. C. C. Drachmann, A. M. Whiticar, E. C. T. O'Farrell, H. J. Suominen, A. Fornieri, T. Wang, G. C. Gardner, C. Thomas, A. T. Hatke, P. Krogstrup, M. J. Manfra, K. Flensberg, and C. M. Marcus, Scaling of Majorana zero-bias conductance peaks, Phys. Rev. Lett. **119**, 136803 (2017).

[16] S. Vaitiekėnas, A. M. Whiticar, M.-T. Deng, F. Krizek, J. E. Sestoft, C. J. Palmstrøm, S. Marti-Sanchez, J. Arbiol, P. Krogstrup, L. Casparis, and C. M. Marcus, Selective-area-grown semiconductor-superconductor hybrids: A basis for topological networks, Phys. Rev. Lett. **121**, 147701 (2018).

[17] S. Matsuo, M. Tateno, Y. Sato, K. Ueda, Y. Takeshige, H. Kamata, J. S. Lee, B. Shojaei, C. J. Palmstrøm, and S. Tarucha, Evaluation of the vortex core size in gate-tunable Josephson junctions in Corbino geometry, Phys. Rev. B **102**, 045301 (2020).

[18] G. C. Ménard, G. L. R. Anselmetti, E. A. Martinez, D. Puglia, F. K. Malinowski, J. S. Lee, S. Choi, M. Pendharkar, C. J. Palmstrøm, K. Flensberg, C. M. Marcus, L. Casparis, and A. P. Higginbotham, Conductance-matrix symmetries of a three-terminal hybrid device, Phys. Rev. Lett. **124**, 036802 (2020).

[19] S. Vaitiekėnas, G. W. Winkler, B. van Heck, T. Karzig, M.-T. Deng, K. Flensberg, L. I. Glazman, C. Nayak, P. Krogstrup, R. M. Lutchyn, and C. M. Marcus, Flux-induced topological superconductivity in full-shell nanowires, Science **367**, eaav3392 (2020).

[20] M. W. A. de Moor, J. D. S. Bommer, D. Xu, G. W. Winkler, A. E. Antipov, A. Bargerbos, G. Wang, N. van Loo, R. L. M. O. het Veld, S. Gazibegovic, D. Car, J. A. Logan, M. Pendharkar, J. S. Lee, E. P. A. M. Bakkers, C. J. Palmstrøm, R. M. Lutchyn, L. P. Kouwenhoven, and H. Zhang, Electric field tunable superconductor-semiconductor coupling in Majorana nanowires, New J. Phys. **20**, 103049 (2018).

[21] J. Shen *et al.*, Parity transitions in the superconducting ground state of hybrid InSb-Al Coulomb islands, Nat. Commun. **9**, 4801 (2018).

[22] G. L. R. Anselmetti, E. A. Martinez, G. C. Ménard, D. Puglia, F. K. Malinowski, J. S. Lee, S. Choi, M. Pendharkar, C. J. Palmstrøm, C. M. Marcus, L. Casparis, and A. P. Higginbotham, End-to-end correlated subgap states in hybrid nanowires, Phys. Rev. B **100**, 205412 (2019).

[23] R. L. M. Op het Veld *et al.*, In-plane selective area InSb-Al nanowire quantum networks, Commun. Phys. **3**, 59 (2020).

[24] T. Kanne *et al.*, Epitaxial Pb on InAs nanowires for quantum devices, Nat. Nanotechnol. **16**, 776 (2021).
[25] M. Pendharkar, B. Zhang, H. Wu, A. Zarassi, P. Zhang, C. P. Dempsey, J. S. Lee, S. D. Harrington, G. Badawy, S. Gazibegovic, R. L. M. O. het Veld, M. Rossi, J. Jung, A.-H. Chen, M. A. Verheijen, M. Hocevar, E. P. A. M. Bakkers, C. J. Palmstrøm, and S. M. Frolov, Parity-preserving and magnetic field-resilient superconductivity in InSb nanowires with Sn shells, Science **372**, 508 (2021).
[26] J. L. N. Tomaszewska, L. Walczak, and J. J. Kolodziej, Surface states and charge accumulation states on reconstructed InAs (001) surfaces, Surf. Sci. **632**, 103 (2015).
[27] S. Schuwalow, N. B. M. Schröter, J. Gukelberger, C. Thomas, V. Strocov, J. Gamble, A. Chikina, M. Caputo, J. Krieger, G. C. Gardner, M. Troyer, G. Aeppli, M. J. Manfra, and P. Krogstrup, Band structure extraction at hybrid narrow-gap semiconductor-metal interfaces, Adv. Sci. **8**, 2003087 (2021).
[28] S. Yang, N. B. M. Schrter, V. N. Strocov, S. Schuwalow, M. Rajpalk, K. Ohtani, P. Krogstrup, G. W. Winkler, J. Gukelberger, D. Gresch, G. Aeppli, R. M. Lutchyn, and N. Marom, Electronic structure of InAs and InSb surfaces: Density functional theory and angle-resolved photoemission spectroscopy, Adv. Quantum Technol. **5**, 2100033 (2022).
[29] R. Batabyal, S. Zelzer, A. P. Romagosa, D. Dardzinski, F. Corsetti, N. Marom, and P. Krogstrup, Origin of surface and subband states at the InAs(111)A surface, Phys. Rev. Mater. **7**, 066201 (2023).
[30] A. V. Krukau, O. A. Vydrov, A. F. Izmaylov, and G. E. Scuseria, Influence of the exchange screening parameter on the performance of screened hybrid functionals, J. Chem. Phys. **125**, 224106 (2006).
[31] QUESTAAL code website, https://www.questaal.org.
[32] S. Smidstrup *et al.*, QuantumATK: An integrated platform of electronic and atomic-scale modelling tools, J. Phys.: Condens. Matter **32**, 015901 (2020).
[33] D. Pashov, S. Acharya, W. R. Lambrecht, J. Jackson, K. D. Belashchenko, A. Chantis, F. Jamet, and M. van Schilfgaarde, Questaal: A package of electronic structure methods based on the linear muffin-tin orbital technique, Comput. Phys. Commun. **249**, 107065 (2020).
[34] S. V. Faleev, M. van Schilfgaarde, and T. Kotani, All-electron self-consistent *GW* approximation: Application to Si, MnO, and NiO, Phys. Rev. Lett. **93**, 126406 (2004).
[35] T. Kotani, M. van Schilfgaarde, and S. V. Faleev, Quasiparticle self-consistent *GW* method: A basis for the independent-particle approximation, Phys. Rev. B **76**, 165106 (2007).
[36] B. Cunningham, M. Grüning, D. Pashov, and M. van Schilfgaarde, QS$G\hat{W}$: Quasiparticle self-consistent *GW* with ladder diagrams in W, Phys. Rev. B **108**, 165104 (2023).
[37] A. L. Kutepov, Self-consistent solution of Hedin's equations: Semiconductors and insulators, Phys. Rev. B **95**, 195120 (2017).
[38] A k-point grid of $(8 \times 6 \times 4)$ was used for the DFT calculations. A smaller grid of $(4 \times 4 \times 2)$ was used for QSGW calculations, with an interpolation scheme to a $(8 \times 6 \times 4)$ grid for the density. The self-consistency of the DFT/QSGW calculations is achieved when the RMS change in output-input self-energy and charge density were both converged to about 5×10^{-6}. For QSGW calculations, all the states are used in the present case (3630 states in the total system, with ≈3200 of them unoccupied). QUESTAAL's basis set is tailored to the potential, so that quasiparticle levels converge much more rapidly with the number of states than occurs in a plane wave basis. Numerous case studies can be found in [46]. Compare convergence for Si to [47].
[39] M. A. L. Marques, J. Vidal, M. J. T. Oliveira, L. Reining, and S. Botti, Density-based mixing parameter for hybrid functionals, Phys. Rev. B **83**, 035119 (2011).
[40] P. Borlido, M. A. L. Marques, and S. Botti, Local hybrid density functional for interfaces, J. Chem. Theory Comput. **14**, 939 (2018).
[41] M. van Setten, M. Giantomassi, E. Bousquet, M. Verstraete, D. Hamann, X. Gonze, and G.-M. Rignanese, The PseudoDojo: Training and grading a 85 element optimized norm-conserving pseudopotential table, Comput. Phys. Commun. **226**, 39 (2018).
[42] M. Guidon, J. Hutter, and J. VandeVondele, Auxiliary density matrix methods for Hartree-Fock exchange calculations, J. Chem. Theory Comput. **6**, 2348 (2010).
[43] J.-W. Luo, A. N. Chantis, M. van Schilfgaarde, G. Bester, and A. Zunger, Discovery of a novel linear-in-k spin splitting for holes in the 2D GaAs/AlAs system, Phys. Rev. Lett. **104**, 066405 (2010).
[44] E. Rashba and E. Sherman, Spin-orbital band splitting in symmetric quantum wells, Phys. Lett. A **129**, 175 (1988).
[45] X. Ren, P. Rinke, V. Blum, J. Wieferink, A. Tkatchenko, A. Sanfilippo, K. Reuter, and M. Scheffler, Resolution-of-identity approach to Hartree-Fock, hybrid density functionals, RPA, MP2 and GW with numeric atom-centered orbital basis functions, New J. Phys. **14**, 053020 (2012).
[46] M. van Schilfgaarde, T. Kotani, and S. V. Faleev, Adequacy of approximations in *GW* theory, Phys. Rev. B **74**, 245125 (2006).
[47] M. L. Tiago, S. Ismail-Beigi, and S. G. Louie, Effect of semicore orbitals on the electronic band gaps of Si, Ge, and GaAs within the *GW* approximation, Phys. Rev. B **69**, 125212 (2004).